Respiration is essential for CO_2 assimilation in marine diatoms

Benjamin Bailleul[1,2,3,4,*], Nicolas Berne[1], Omer Murik[4], Dimitris Petroutsos[5], Judit Prihoda[4], Atsuko Tanaka[4], Valeria Villanova[6], Richard Bligny[5], Serena Flori[5], Denis Falconet[5], Anja Krieger-Liskay[7], Stefano Santabarbara[8], Fabrice Rappaport[3], Pierre Joliot[3], Leila Tirichine[4], Paul Falkowski[2], Pierre Cardol[1], Chris Bowler[4,*], Giovanni Finazzi[5,*]

1 Genetics and Physiology of Microalgae, Department of Life Sciences, University of Liège, B-4000 Liège, Belgium; PhytoSYSTEMS, University of Liège, B-4000 Liège, Belgium.

2 Environmental Biophysics and Molecular Ecology Program, Department of Marine and Coastal Sciences and Department of Earth and Planetary Sciences, Rutgers University, New Brunswick, NJ 08901, USA

3 Institut de Biologie Physico-Chimique (IBPC), Centre National de la Recherche Scientifique (CNRS), UMR 7141, Université Pierre et Marie Curie, 13 Rue Pierre et Marie Curie, 75005 Paris, France

4 Institut de Biologie de l'Ecole Normale Supérieure (IBENS), Centre National de la Recherche Scientifique (CNRS) UMR 8197 INSERM U1024, 46 Rue d'Ulm, 75005 Paris, France

5 Laboratoire de Physiologie Cellulaire et Végétale, UMR 5168, Centre National de la Recherche Scientifique (CNRS)-Commissariat à l'Energie Atomique-Université Grenoble Alpes, Institut de Recherche en Sciences et Technologies pour le Vivant, Commissariat à l'Energie Atomique (CEA) Grenoble, 38054 Grenoble cedex 9, France

6 Fermentalg SA, F-33500 Libourne, France

7 Institute for Integrative Biology of the Cell (I2BC), Commissariat à l'Energie Atomique et aux Energies Alternatives (CEA) Saclay, Institut de Biologie et de Technologie de Saclay, Centre National de la Recherche Scientifique (CNRS), Université Paris-Sud, F-91191 Gif-sur-Yvette cedex, France

8 Istituto di Biofisica, Consiglio Nazionale delle Ricerche, Via Celoria 26, 20133 Milan, Italy

* Corresponding author

Over the past ~ 35 million years, diatoms have been one of the most successful classes of photosynthetic marine eukaryotes, and are believed to have contributed to climate cooling by absorbing carbon dioxide from the atmosphere and sequestering it in the ocean interior via the biological carbon pump[1]. Today their contribution to planetary primary production is equivalent to that of terrestrial rainforests[2]. Diatoms are secondary endosymbiotic algae derived from a complex evolutionary history[3] that show an outstanding capacity for photosynthetic CO_2 assimilation in response to nutrient "shift-up" events[4]. Here we show that photosynthesis in diatoms occurs via extensive energetic exchanges between the plastids and mitochondria. Unlike all other obligate

photosynthetic organisms characterized to date, rerouting of reducing power generated in the plastid to mitochondria, and the import of mitochondrial ATP, are mandatory for photosynthesis. Impaired mitochondrial activity results in ATP shortage and enhanced accumulation of reducing equivalents in the plastids, leading to a decreased photosynthetic activity and reduced growth. Our work indicates that in diatoms metabolic exchanges between mitochondria and plastids optimize the ATP/NADPH ratio for enhancing the efficiency of light conversion into organic matter.

In oxygenic photosynthesis, light drives ATP and NADPH synthesis via linear electron flow (LEF), requiring the in-series activity of the two photosystems (PS): PS1 and PS2. However, theoretical analyses of the two energetic products suggest that ATP production per NADPH is not sufficient for carbon assimilation in the Calvin-Benson-Bassham (CBB) cycle[5]. Additional ATP is therefore produced by alternative electron pathways (AEPs), capable of generating an electrochemical proton gradient ($\Delta\mu_H^+$ or proton motive force, PMF) without NADPH synthesis. In microalgae, AEPs typically represent only a small fraction of the linear electron flow (typically ~10%)[6], but they have an essential role in optimizing CO_2 assimilation. Because it is currently unknown what mechanisms are utilized by diatoms to balance the energetic needs of carbon fixation, we used a range of techniques to investigate the process in the model diatom *Phaeodactylum tricornutum*.

The PMF generated across thylakoid membranes comprises an electrical ($\Delta\Psi$) and an osmotic (ΔpH) component. The $\Delta\Psi$ can be probed *in vivo* by measuring the ElectroChromic Shift (ECS) of photosynthetic pigments, a change in their absorption spectrum caused by the change in transmembrane electric field[7]. As shown in Extended Data Fig. 1a, an ECS signal is visible in *P. tricornutum,* the characteristics of which depend on the physiological conditions. Deconvolution of the ECS decay-associated spectra (DAS) (see Supplementary Information and Extended Data Fig. 1b,c) explains these observations by revealing the existence of two ECS components (Fig. 1a), respectively characterized by linear and quadratic responses to the $\Delta\Psi$ (Fig. 1b). The existence of a quadratic ECS, predicted by theory[7] but observed to date only in green algae mutants[8], provides *P. tricornutum* cells with an 'internal voltmeter' that we exploited to probe he PMF *in vivo*. The amplitude of the quadratic ECS is a parabolic function of the linear ECS (Fig. 1c, d, e and Extended Data Fig. 1d, e, f). However, upon dark relaxation of the light-induced ECS, the signal does not relax to the minimum of the parabola, but rather to an intermediate level, indicating the persistence of a PMF across the photosynthetic membranes in the dark ($\Delta\Psi_d$; Fig. 1c,d, e). As expected, the $\Delta\Psi_d$ collapsed upon dissipation of the PMF with an ionophore (Fig. 1c), but was also suppressed by anaerobiosis or by pharmacological inhibition of mitochondrial activity (Fig. 1d, e). This suggests that the PMF is generated in the dark by the plastidial ATPase, which hydrolyses ATP of mitochondrial origin, as previously suggested in green algae[9].

In *Viridiplantae* (including green algae and higher plants), the AEPs generating additional ATP in the light comprise cyclic electron flow (CEF) around PS1[10] and the water-to-water cycles (WWC). The latter processes include the Mehler reaction at the PS1 acceptor side[11], the activity of the plastoquinone terminal oxidase downstream of PS2[12], the oxygenase activity of RuBisCO (photorespiration[13]) and, more broadly, the export of reducing equivalents (NADPH) towards the mitochondrial oxidases through the malate shuttle[14]. We first evaluated spectroscopically the possible role of CEF in *P. tricornutum in vivo*. CEF capacity represented only ~5% of the maximum electron flow (Fig. 2a and Extended Data Fig. 2a, c). We also looked for a possible *in vivo* role of the WWC in the light using membrane-inlet mass spectrometry (MIMS) on cells incubated with $^{18}O_2$. O_2 uptake (U_0) increased with light, being ~2.5-fold higher at saturating light intensities than in the dark (Extended Data Fig. 2b, d). We further found that the light-stimulated consumption of oxygen was blocked by DCMU (Extended Data Fig. 2c, d), indicating that it was fed by electrons derived from PS2. Moreover, U_0 linearly increased with O_2 evolution, in agreement with earlier findings in the diatom *Thalassiosira pseudonana*[15], with a slope indicating that ~10% of the electron flow from PSII participate in WWC, regardless of light intensity (Fig 2b). These results indicate that WWC produces a constant extra ATP per photosynthetically-generated NADPH. This is expected for an AEP that contributes to optimizing CO_2 assimilation at any light intensity, and is not the case for CEF, which is completely insensitive to changes in the photosynthetic flux (LEF, Fig 2a).

If this WWC is due to the export of photosynthetic products towards the mitochondrial oxidases, then any mitochondrial dysfunction should negatively affect photosynthetic electron transfer rates (ETR_{PSII}) and light-dependent growth. Mitochondrial respiration comprises a cyanide-sensitive pathway (involving Complex III) and an insensitive pathway involving the alternative oxidase (AOX). We therefore modulated mitochondrial activity by adding increasing amounts of Antimycin A (AA) or myxothiazol (Mx), inhibitors of Complex III, in conditions where the AOX was inhibited by SHAM (see legend to Fig. 2d). Both the $\Delta\Psi_d$ and ETR_{PSII} followed respiration linearly (Fig. 2c, d and Extended Data Fig. 3). The almost complete shut-down of respiration resulted in a decrease of photosynthesis which was independent of light intensity (Fig. 3b).

Overall we found that in the dark a PMF is generated in the plastid by hydrolysis of ATP produced in mitochondria (Fig 1d,e and Fig. 2c). Conversely, in the light, respiration increases linearly with photosynthesis (Fig. 2b), and vice versa (Fig. 2d). This tight energetic coupling is likely instrumental for adjusting the ATP/NADPH ratio to match the demands of carbon fixation (Fig. 2e). Moreover we observed that the sensitivity of photosynthesis (ETR_{PSII}) to SHAM increased with light, suggesting that the AOX pathway becomes prevalent in high light (Fig. 3b). This prompted us to generate AOX knockdown cell lines of *P. tricornutum*. Two independent clones were selected based on reduced protein accumulation (Fig. 3a) and decreased AOX activity (measured as the SHAM-sensitive fraction of respiration; Extended Data Fig. 4a). The AOX contribution, representing ~50% of dark respiration in wild-type cells (Extended Data Fig. 3d), was decreased by 2-fold in the two knockdown lines. Confocal microscopy confirmed the mitochondrial localization of the targeted gene product (Extended Data Fig. 5a). The reduced AOX activity in the knockdown lines paralleled a diminished PMF in the dark, and this effect was strongly enhanced by addition of AA (Extended Data Fig. 4b), despite the fact that dark respiration was slightly higher (Extended Data Fig. 4a). The decreased AOX activity correlated with a decreased photosynthetic capacity, especially under high light intensities (similar to SHAM-treated wild-type cells; Fig. 3b). Reduced photosynthesis translated into a diminished growth rate (Fig. 3c), which was exacerbated by further inhibiting respiration using AA (Extended Data Fig. 6a). This growth phenotype was not due to changes in the composition of the photosynthetic apparatus (Fig. 3a), which was comparable in the wild-type and mutant lines, the only exception being a small apparent decrease in the Cytochrome *f* content, suggesting a possible decrease in the Cytochrome b_6f content of the cells. However, this did not translate into any detectable decrease in the catalytic capacity of the complex (Extended Data Fig. 7), excluding changes in the activity of the photosynthetic complexes as the cause of the observed decrease in photosynthetic performance. Moreover, no detectable differences were seen in the responses to excess light, mediated by so called high energy quenching (NPQ; Extended Data Fig. 6b).

According to our working model (Fig. 2e), partial disruption of the plastid-mitochondria interaction in the knockdown lines should lead, in the light, to the accumulation of NADPH and, complementarily, to a decreased cellular content of ATP. *In vivo* assessments of the pools of NADPH (Fig. 3d and Extended Data Fig. 8a) and ATP (Fig. 3e and Extended Data Fig. 8b) in wild-type and knockdown cell lines confirmed these expectations. The increase of the NADPH/NADP$^+$ ratio with light intensity (Fig. 3d), as well as the net decrease of cellular ATP levels in the light, further enhanced in the presence of AA (Fig. 3e), suggest that CO_2 fixation is limited by ATP availability in both wild-type and mutant cells. Moreover, the NADPH pool reached saturation at lower light intensities and the decrease of ATP in the light was more drastic in mutant cells. These observations confirm that mitochondrial respiration directly participates in the adjustment of the ATP to NADPH ratio. The observation of similar ECS features (linear and quadratic ECS probes) in other diatoms, including *Thalassiosira pseudonana* and *T. weissflogii*, *Fragilaria pinata* and *Ditylum brightwelii* (Fig. 4a), confirmed the presence of a PMF in the plastids in the dark at the expense of hydrolysis of ATP supplied by the mitochondria in all cases (Fig. 4b). Moreover, a negligible contribution of CEF (Extended Data Fig. 9) and a significant involvement of mitochondrial respiration (Extended Data Fig. 10) to photosynthesis were found in all these species, consistent with the findings in *P. tricornutum*.

Thus, the involvement of mitochondrial respiration in the optimization of photosynthesis appears to be a general and conserved feature in diatoms.

We conclude that ATP limits photosynthetic carbon assimilation in diatoms, as reported in other photosynthetic organisms, but that the rerouting of reducing power towards mitochondria allows the production of additional ATP required to optimize primary productivity[5]. In the dark, this ATP is hydrolyzed to generate a PMF in the plastids (Fig. 1d), while in the light it is used in CO_2 assimilation to compensate for the shortage of ATP from LEF (Fig. 2d). Such a system is unlikely to occur in plants, where CEF allows ATP-to-NADPH adjustments[10] while the malate shunt and AOX are considered as a safety valve for dissipating excess reductants[13]. However the potential for mitochondrial metabolism dependent $C0_2$ fixation was documented in green algae upon disruption of CEF[9,16] or inhibition of plastidial ATP synthesis[17], suggesting that the process can exist in other unicellular photosynthetic eukaryotes in non-physiological conditions.

The underpinnings of the process described herein could stem from the complex evolutionary history of diatoms as secondary endosymbionts, proposed to be derived from the incorporation of green and red algae into a heterotrophic eukaryote[3], leading to the evolution of novel metabolisms, as previously highlighted by the discovery of a fully functional ornithine-urea cycle[18]. The extensive interactions between diatom plastids and mitochondria observed here imply the significant exchange of reducing equivalents and ATP between the two compartments, despite the fact that diatom plastids are surrounded by four instead of two membranes. The very tight physical interactions observed between plastids and mitochondria in diatoms (Extended Data Fig. 5b) likely facilitate exchanges through redox carriers such as STI1 and DiT2[19], as well as OMT/Dit1, the chloroplast component of the plant malate shuttle[14], all of which are encoded in the *P. tricornutum* genome[20]. The capacity to share ATP in the light between the two organelles could provide a means not only to optimize CO_2 assimilation but also to activate photosynthesis during nutrient shift-up events, a key issue underlying the impressive performance of diatoms in contemporary oceans.

Acknowledgements

This work was supported by grants from Agence Nationale de la Recherche (ANR-12-BIME-0005, DiaDomOil to CB and GF and ANR-8NT09567009, Phytadapt to BB, GF and CB), the CNRS Défi Transition énergétique : ressources, société, environnement (ENRS) to GF and LT, the Région Rhône-Alpes (Cible project) to GF, the Marie Curie Initial Training Network Accliphot (FP7-PEPOPLE-2012-ITN; 316427) to GF, DP, SF, and VV, an ERC Advanced Award (Diatomite) to CB. PC, NB, and BB acknowledge financial support from the Belgian Fonds de la Recherche Scientifique F.R.S.-F.N.R.S. (F.R.F.C. 2.4597.11, CDR J.0032.15, and Incentive Grant for Scientific Research F.4520). BB also acknowledges a post-doctoral fellowship from Rutgers University. Thanks are due to Jean-Luc Putaux and Christine Lancelon-Pin of the CERMAV institute (Grenoble) for allowing us to use the UC6 Leica ultramicrotome and to Lucas Moyet (LPCV) for helpful technical support in the preparation of samples for the in vivo NMR analysis.

References

1- PG, Falkowski (2004) The evolution of modern eukaryotic phytoplankton. Science **305**: 354-360.

2- CB, Field, MJ, Behrenfeld, JT, Randerson, PG, Falkowski (1998) Primary production of the biosphere: Integrating terrestrial and oceanic components. Science **281**: 237–240.

3- A, Moustafa et al (2009) Genomic footprints of a cryptic plastid endosymbiosis in diatoms. Science **324**: 1724-1726.

4- EV, Armbrust (2009) The life of diatoms in the world's oceans. Nature **459**: 185-192.

5- JF, Allen (2002) Photosynthesis of ATP-Electrons, proton pumps, rotors, and poise. Cell **110:** 273-276.

6- P, Cardol et al (2009) Impaired respiration discloses the physiological significance of state transitions in Chlamydomonas. Proc. Natl. Acad. Sci. USA **106**: 15979-15984.

7- HT, Witt (1979) Energy conversion in the functional membrane of photosynthesis. Analysis by light pulse and electric pulse methods. The central role of the electric field. Biochim. Biophys. Acta **505**: 355-427.

8- P, Joliot, A, Joliot (1989) Characterization of linear and quadratic electrochromic probes in *Chlorella sorokiniana* and *Chlamydomonas reinhardtii*. Biochim. Biophys. Acta **9753**: 355-360.

9- B, Diner, P, Joliot (1967) Effect of the transmembrane electric field on the photochemical and quenching properties of photosystem II *in vivo*. Biochim. Biophys. Acta **423**: 479-498.

10- T, Shikanai (2007) Cyclic electron transport around Photosystem I: Genetic approaches. Annual Review of Plant Biology **58**: 199-217.

11- K, Asada (2000) The water-water cycle as alternative photon and electron sinks. Philos. Trans. R. Soc. Lond. B. Biol. Sci. **355**: 1419-1431.

12- JP, Zehr, RM, Kundela (2009) Photosynthesis in the open ocean. Science **326**: 945-946.

13- DR, Ort, NR, Baker (2002) A photoprotective role of O_2 as an alternative electron sink in photosynthesis? Current Opinion in Plant Biology **5**: 193-198.

14- H, Kinoshita et al (2011) The chloroplastic 2-oxoglutarate/malate transporter has dual function as the malate valve and in carbon/nitrogen metabolism. Plant J. **65**: 15-26.

15- J, Waring, M, Klenell, G, Bechtold, JC, Underwood and N, Baker (2010) Light- induced responses of oxygen photo- reduction, reactive oxygen species production and scavenging in two diatom species. J. Phycol. **46**: 1206–1217.

16- KV, Dang et al (2014) Combined increases in mitochondrial cooperation and oxygen photoreduction compensatefor deficiency in cyclic electron flow in *Chlamydomonas reinhardtii*. Plant Cell **26**: 3036-3050.

17- C, Lemaire, FA, Wollman, P, Bennoun (1988) Restoration of phototrophic growth in a mutant of *Chlamydomonas reinhardtii* in which the chloroplast atpB gene of the ATP synthase has a deletion: an example of mitochondria-dependent photosynthesis. Proc Natl Acad Sci U S A. **85**: 1344-1348.

18- AE, Allen et al (2011) Evolution and metabolic significance of the urea cycle in photosynthetic diatoms. Nature. **473**: 203-207.

19- AP, Weber, N, Linka (2011) Connecting the plastid: transporters of the plastid envelope and their role in linking plastidial with cytosolic metabolism. Annu. Rev. Plant. Biol. **62**: 53-77.

20- J, Prihoda et al (2012) Chloroplast-mitochondria cross-talk in diatoms. J Exp Bot. **64**: 1543-1457.

Figure Legends

Figure 1. ECS provides an internal voltmeter in *P. tricornutum.*

a. Decay associated spectra of the ElectroChromic Signal (ECS) spectrum. Spectra were calculated from data in Extended Data Fig. 1b,c, as described in Supplementary Information. **b.** Schematic representation of polar (blue) and polarizable (red) pigments, and theoretical dependencies of their associated ECS responses upon the ΔΨ. **c. d. e.** Relationship between the quadratic ECS and the linear ECS (see Extended Data Fig.1d,e,f and Supplementary Information) in control (open symbols) and in the presence of ionophores (FCCP 8nM, **c**), in anaerobic conditions (**d**), and in the presence of respiratory inhibitors (AA, 5µM, and SHAM, 1mM, **e**) (closed symbols). The value of the dark $\Delta\Psi$ ($\Delta\Psi_d$) is shown by a green arrow. By calibrating the linear ECS with the signal induced by a saturating flash (i.e., a charge separation in the photosystems; see Supplementary Information), we quantified the $\Delta\Psi_d$ as ~ 5 charge separations by PS1, i.e., 100 mV ca (Witt, 1979).

Figure 2. Mitochondria-plastid energetic interactions in *P. tricornutum.*

a. b. Relationship between CEF capacity and linear electron flow (**a**) and between oxygen uptake (U_0) and gross photosynthesis (E_0) as measured by MIMS (**b**) in *P. tricornutum.* Points correspond to the data presented in Extended Data Fig. 2c,d. **c. d.** Dependency of dark PMF ($\Delta\Psi_{dark}$; **c**) and photosynthetic activity (ETR_{PSII}; **d**) on the respiration rate. Open and closed circles in panel **d** correspond to SHAM +AA or SHAM +Mx treatments, respectively. Points correspond to the data presented Extended Data Fig. 3a,b,c. **e.** Schematic representation of possible plastid-mitochondria metabolic interactions. Lines represent LEF (light blue), CEF (dark blue) and respiratory (red) electron transfer. Dashed lines indicate putative exchange pathways between the organelles for reducing equivalents (orange) and ATP (brown). PMF is indicated in green. PS= photosystem, b_6f=cytochrome *b_6f*, ATPase=ATP ase/synthase, CBB cycle=Calvin-Benson-Bassham cycle, I/ III/ IV = complexes 1, 3 and 4, and AOX=Alternative Oxidase.

Figure 3. Phenotypic traits of AOX mutants in *P. tricornutum.*

a. Western blot analysis of photosynthetic and respiratory complexes using specific antibodies. **b**. Sensitivity of photosynthetic activity to inhibitors of respiration. Relative decrease of ETR_{PSII} is presented for wild-type cells incubated with AA (blue stars), SHAM (red triangles) and AA+SHAM (black circles), compared to control conditions. Data refer to two independent experiments ± standard deviation (±S.D.). Green and magenta circles represent inhibition of photosynthesis in kd-c5 and kd-c9 AOX mutants, respectively, compared to wild type (5 independent experiments ± standard deviation). **c**. Growth rates of the wild type (dark blue) and AOX knockdown mutants (magenta and green) (7 independent experiments ± S.D.). **d**. *In vivo* assessment of NADPH redox state, as a function of light intensity, in wild-type and AOX knockdown mutants (same color code as **c**, data from Extended Data Fig. 8a). Data represent the averages from three independent experiments (± S.D.). **e**. *In vivo* 31P-NMR evaluation of the NTP content in wild-type and AOX knockdown mutant cells, in the dark or in low light (with or without AA). See Extended Data Fig. 8b for more information.

Fig 4. ATP transfer from mitochondria to plastid in representative diatoms.

a. Spectra of the linear (blue circles) and quadratic (red circles) ECS probes in *T. weissflogii*, *T. pseudonana*, *F. pinnata* and *D. brightwelii*. See Supplementary Information for more details. **b**. Relationship between the quadratic and the linear ECS in control conditions (open green squares) and in the presence (closed green circles) of respiratory inhibitors AA (5µM) and SHAM (500µM). The data presented are representative of 4-8 independent experiments (± S.D.).

Supplementary Information

Methods

Culturing: Wild type and AOX transformant lines of *Phaeodactylum tricornutum* Pt1.86 (CCMP2561) were grown in artificial sea water (ASW[1]). *Thalassiosira pseudonana* (CCMP1335), *Thalassiosira weissflogii* (CCMP1336), *Fragilaria pinata* (CCAP 1029/2) and *Ditylum brightwelii* (CCMP359) were grown in F/2 medium, supplemented with silica[2]. All strains were grown at 19±1 °C, in semi-continuous batch culture with moderate shaking. The photoperiod was 12 hours light/12 hours dark, and light intensity was 70µmol photons m^{-2} s^{-1}, unless otherwise stated. Cell concentration was determined daily with a Z2 Coulter Counter analyzer (Beckman Coulter), to ensure all the experiments were performed in exponential phase. For biophysical measurements, cells were concentrated by centrifugation, resuspended in their growth medium (supplemented with 10% w/v Ficoll for absorption spectroscopy to prevent cell sedimentation), and kept in the dark at least 30 minutes before measurements.

Inhibitors: DCMU, FCCP, Antimycin A, Myxothiazol and SHAM (Sigma-Aldrich, Munich, Germany) were dissolved in ethanol, whereas HA, glucose, glucose oxidase and catalase (Sigma-Aldrich, Munich, Germany) were dissolved in deionized water. FCCP was used at a very low concentration (8 nM) to allow the disruption of the dark PMF without preventing the light-induced generation of PMF needed for the measurement of the $\Delta\Psi_{dark.}$ Antimycin A and Myxothiazol were used at 5µM, unless otherwise stated (Extended Data Fig. 3). DCMU was used at a concentration of 15µM. : For each measurement involving HA or SHAM, we used the lowest concentration allowing in each strain a full inhibition of PSII activity or a maximal inhibition of respiration, respectively. The range of concentration used was 30-100µM and 500-1000µM for HA and SHAM, respectively. Anaerobic conditions were obtained through incubation with catalase (1000 U/mL), glucose (10 mM) and glucose oxidase (2 mg/mL).

Absorption spectroscopy: Absorption difference signals were measured at different wavelengths with a Joliot-type spectrophotometer (JTS-10, Biologic), equipped with a white probing LED and the adequate interference filters (3 to 8 nm bandwidth). All data were normalized to the increase of linear ECS upon a saturating laser flash (i.e., 1 charge separation per photosystem). The actinic flash (~7 ns) was provided by a laser dye (LDS 144 698) pumped by a double frequency Nd-YAG laser (Quantel, Brilliant). For ΔΨ measurements, the PMF was increased using a ~10ms pulse of saturating (4500 µmol photons.m^{-2}.s^{-1}) red light (see Extended Data Fig. 1 for representative ECS kinetics) or a series of 6 laser flashes (for Fig. 1a and Extended Data Fig. 1A only). For *P. tricornutum*, ecs_{lin} and ecs_{quad} were first evaluated using a 3 wavelength deconvolution, to minimize contribution from Cytochrome *c* (see Extended Data Fig. 1c, d, e, f). Cyt. *c* = [554]-0,4*[520]-0,4*[566], ecs_{lin}=[520]-0,25*Cyt. *c* and ecs_{quad}=[566]+0,15*Cyt. *c*. For the other diatoms, appropriate wavelengths were chosen for linear and quadratic ECS to minimize the cytochrome contributions (red and blue lines in Fig. 4). The relationships between ecs_{lin} and ecs_{quad} were then fitted with the parabolic equation $ecs_{quad} + a*b^2 = a*(ecs_{lin}+b)$, where b is the ΔΨ in the dark ($\Delta\Psi_{dark}$ expressed in charge separation per PS) and a is constant for all the experiments related to a diatom species. The ecs_{lin} and ecs_{quad} were then corrected for the dark electric field (see Extended Data Figure 1f, top panel) to allow a better comparison between different physiological conditions: $ECS_{lin} = ecs_{lin} + b$, and $ECS_{quad} = ecs_{quad} + a*b^2$. This simply corresponds to a shift of the x and y axis to allow the minimum of the parabola to coincide with the origin of the axes (see Extended Data Figure 1f, top panel).

Cyt *b6f* turnover was measured though the slow phase (phase b) of the ECS, which reflects b6f-catalysed charge transfer across the membranes, and through the reduction rate of the cyt. *c/f ,* both measurements being performed after a saturating laser flash.

For calculation of the total electron flow (TEF) and cyclic electron flow (CEF) capacity (Fig. 2A), we measured the photochemical rates in the absence and presence, respectively, of DCMU. In brief, under steady state illumination conditions the ECS signal results from concomitant transmembrane potential generation by PS2, the cytochrome b_6f complex and PS1 and from transmembrane potential dissipation by the ATP synthase CF_0-F_1. When light is switched off, reaction center activity stops immediately, while ATPase and the cytochrome b_6f complex activities remain (transiently) unchanged. Therefore, the difference between the slopes of the ECS signal measured in the light (s_L) and after the light is switched off (s_D) is proportional to the rate of PS1 and PS2 photochemistry (i.e., to the rate of “total’ electron flow). This can be calculated by dividing this slope by the linear ECS signal induced by a saturating laser flash (see[3]) to evaluate the number of charge separations per photosystem and per second. The rate of CEF can be evaluated using the same approach under conditions where PS2 activity is inhibited by DCMU.

Linear and quadratic ECS deconvolution: For the deconvolution of the linear and quadratic contributions to the ECS signals, we considered that the relaxation of the electric field generated by a light perturbation can be described by the exponential function: $\Delta\Psi = \Delta\Psi0*\exp[-t/\tau]$, where t is time, ΔΨ0 is the initial electric field generated by the light, and τ is the electric field decay lifetime. The linear and quadratic components of the ECS are proportional to ΔΨ and $\Delta\Psi^2$ respectively. Therefore, the ΔI/I spectro- temporal matrixes (from 460 to 600 nm) can be described by a sum of two exponentials: $y(\lambda, t) = A(\lambda).\exp(-t/\tau) + B(\lambda).\exp(-2.t/\tau) + C(\lambda)$. The kinetics of ECS relaxation were fitted by a global routine, which consider the lifetime τ (common to the linear and quadratic ECS components) as a global (wavelength independent) variable, and the amplitudes of linear and quadratic components (A and B, respectively) as local (wavelength dependent) variables. A non-decaying component (C) was also included in the fit to account for a small fraction of residual signal at long delay times. The plot of the A and B amplitudes as a function of the detection wavelength provides the Decay Associated Spectra (DAS) of the linear and quadratic contributions to the ECS signal, respectively. The fit was performed by a laboratory written software minimising the reduced sum of squared residues between the model function and the experimental data, employing a two-steps protocol involving an initial search that utilises the Simplex method (Nelder-Mead algorithm) and a refined search using the Levenberg-Marquardt algorithm as described in[4], but using the MINUIT package, developed and distributed by CERN, Genevra, Switzerland, implemented in FORTAN77. The quality of the fit description was judged on the basis of reduced sum of squared residues statistics, visual inspection of the fit residuals, residuals autocorrelation and stability of the solutions upon random perturbation of the best-fit.

Fluorescence- based measurements: Fluorescence-based photosynthetic parameters were measured on a fluorescence imaging setup described in[5]. Photosynthetic electron transfer rate ETR_{PSII} and NPQ were calculated, respectively, as (Fm'-F)/Fm'*I and (Fm-Fm')/Fm', where F and Fm' are the fluorescence intensities, respectively, in steady state light and after a saturating pulse in the light acclimated cells, Fm is the maximal fluorescence intensity in dark-adapted cells, and I is the light irradiance in µmol photons/m^2/s (Genty, 1989[6]). The light saturation curves of ETR_{PSII} were fitted with the exponential rise function $P = P_{max}$ (1-exp(E/E_k)), where P_{max} is the maximal photosynthetic electron transport rate and E_k is the optimal light. ΔETR (Fig 3b) was calculated as (ETR_{ref}-ETR)*100/ ETR_{ref}, the references being the wt in control conditions.

Respiration rates were measured as O_2 exchange rates using a Clark-type oxygen electrode at 19°C (Hansatech Instrument, King's Lynn, England). AOX capacity was measured as SHAM-sensitive respiration in conditions where the cyanide-sensitive pathway was inhibited (AA, 5µM).

ATP/NADPH *in vivo* measurements: NADP+/NADPH redox changes were followed in living cells using a dual PAM (Walz, germany). NADPH fluorescence was measured at 460 nm, upon excitation in the near UV. Chlorophyll *a* concentration was ~5µg/mL. ATP content was measured using an *in vivo* ^{31}P-AMX 400 NMR spectrometer equipped with a 25-mm multinuclear probe tuned at 161.9 MHz, and a home-made lighting system, as described in[7]. The relative ATP content was estimated *in vivo* from the surface of α-, β- and γ-phosphorus resonance peaks corresponding to the three phosphates of NTPs, which dominate the NMR spectra with inorganic phosphate and polyphosphates[8].

Western blots and immunolocalization :
Protein samples (5-10 µg) were loaded on 13% SDS-PAGE gels and blotted to nitrocellulose. Primary AOX antibody was customly designed (Sdix, USA, 1:4000 dilution). All other antisera used were obtained from Agrisera (Vännäs, Sweden). The blots were developed with ECL detection reagent and images of the blots were obtained using a CCD imager (Chemidock MP Imaging, Bio-Rad).

Immunolocalization of AOX was generally done as described in[9]. Briefly, cells were fixed with 2% formaldehyde in culture media for 20 minutes , washed 3 times with marine phosphate buffer (mPBS, see[9]) and premeabelized by 1% Triton X-100 in mPBS for 10 minutes. The cells were washed again, blocked for 30 minutes in 1% BSA in mPBS and incubated over night at room temperature with anti-AOX antibody from rabbit (custom design, Sdix, USA, 1:200 dilution in mPBS). The cells then were rinsed with mPBS and incubated with donkey Alexa 488-conjugated anti-rabbit IgG antibody (Life Technologies, USA, at 1:100 dilution in mPBS) for 2 h at room temperature. Cells were then stained with 0.5µg/ml DAPI (4',6'-diamidino-2-phenylindole, Life technologies) for 10 min and mounted with Vectashield (Vector Laboratories, Inc., USA) after a rinse. Finally the cells were observed using a Leica SP5 confocal microscope (Leica Microsystems, Germany).

Membrane inlet mass spectrometer (MIMS) measurements: Samples were introduced in a 3 mL thermostated cuvette, which was connected to a Quadrupole Mass Spectrometer (QMS 200, Pfeiffer Vacuum Prisma, Asslar, Germany) by a stainless steel vacuum tube (1/8 inch) passing through a water trap filled with ethanol and dry ice. The sample was separated from the tube via a gas permeable inlet system (PTFE membrane). $^{18}O_2$ was added as a bubble to the algal suspension, and the bubble was removed prior to the experiment. The measurements of the partial pressure of $^{16}O_2$ ($P^{16}O_2$, m/z = 32), $^{18}O_2$ ($P^{18}O_2$, m/z =36) and Argon (m/z =40) were performed after the cuvette was sealed. A blue LED source was connected to the cuvette, and the light intensity was manually adjustable in the 0 to ~800 µE/m2/s range. The temperature was kept at 19 ± 1 °C in the cuvette during the experiment.

To calculate gross O_2 production (E_0) and uptake (U_0), respectively, production and consumption by the cells, we adapted the equations from[10],

$U_0 = (\Delta[^{18}O]/\Delta t + k[^{18}O])*([^{18}O]+[^{16}O]/[^{18}O])$

$E_0 = (\Delta[^{16}O]/\Delta t + k[^{16}O]) + U0*([^{18}O]+[^{16}O]/[^{16}O])$

Where k is the rate constant of O_2 decrease measured in the absence of algae. We normalized O_2 to Argon- a biologically inert gas with very similar solubility properties, which decreases the sensitivity of O_2 measurements to fluctuations by ~80% (Kana et al. 1994[11]). The gas concentrations were calibrated by measuring air-equilibrated O_2 concentration (stirring deionized water in the open cuvette for at least 5 hours) and background O_2 (bubbling with N_2).

Electron microscopy: For transmission electron microscopy (TEM), *P. tricornutum* cells were fixed in 0.1 M cacodylate buffer (Sigma-Aldrich) pH 7.4 Containing 2.5% glutaraldehyde (TAAB), 2% formaldehyde (Polysciences, Inc.) for one hour at room temperature and then prepared according to a modified protocol from Deerinck et al. (Deerinck, T.J. et al. http://ncmir.ucsd.edu/ sbfsem-protocol). After the dehydration steps, the cells were infiltrated with ethanol/Epon resin mixture (2/3-1/3 for one hour and 1/3-2/3 for one hour) and finally embedded in Epon in a 60°C oven for 48 hours or longer. Ultrathin sections (60 nm) were prepared with a diamond knife on an UC6 Leica ultramicrotome and collected on 200 µm mesh nickel grids before examining on a JEOL 1200 EX electron microscope.

Extended Data Figures

Extended Data Fig. 1. Characterization of the ECS- based internal voltmeter.

a. ECS spectra in aerobic (closed circles) and anaerobic (open circles) conditions (see Supplementary Information). **b**. Absorption difference (ΔI/I) kinetics followed at different wavelengths in *P. tricornutum,* after a series of six saturating laser flashes, in anaerobic conditions. Solid lines correspond to the global fit of the experimental data with a sum of two exponential decays, with time constants τ and $2*\tau$ respectively, as expected for linear and quadratic dependencies (see Methods). **c**. ΔI/I spectra are shown at different times during ECS relaxation. All spectra were normalized to 1 at 520 nm to allow better comparison. The observation that most of the spectrum is homothetic during relaxation, while changes are seen in the red most part of the signal suggests the presence of two components, having different relaxation kinetics. **d**. Kinetics of ΔI/I changes at 520, 554 and 566 nm during a ~10ms pulse of saturating red light (4000 µmol. photons.$m^{-2}.s^{-1}$) and the subsequent dark relaxation (top: control conditions, bottom: AA+SHAM). **e**. Kinetics of changes of ecs_{lin}, ecs_{quad} and c-type cytochrome redox state, from kinetics in panel **d**, after the deconvolution procedure described in Supplementary Information. The fast relaxation of c-type cytochromes in both conditions, despite very different ECS relaxations, validates the deconvolution procedure. **f**. Relationship between the quadratic and the linear ECS (ecs_{lin}, ecs_{quad} from panel **e**). In the top panel (and also in Fig. 1e), the green circles and squares correspond to the data before and after correction for the dark electric field, respectively (see methods). The green arrow indicates the value of the electric field in the dark in control conditions.

Extended Data Fig. 2. Cyclic electron flow and water-to-water cycles in *P. tricornutum.*

a. Representative traces of changes in linear ECS (normalized as explained in Supplementary Information) to evaluate linear and cyclic electron flow. Cells were illuminated with 1870 µE/m^2/s of red light, in the presence (open circles) and absence (closed circles) of DCMU and then transferred to the dark. Traces represent changes in the linear ECS. To quantify LEF and CEF, the difference between the slopes of the ECS changes in the light (s_L) and in the dark (S_D) was normalized to the amplitude of the 1 charge separation by PS1, i.e., the ECS measured in samples treated with DCMU and hydroxylamine (1 mM) to fully block PS2 activity . **b**. Representative traces of the $^{16}O_2$ and $^{18}O_2$ concentrations at the offset of a 280 µE/m^2/s blue light. In panels **a** and **b**, light and dark periods are represented by yellow and black boxes, respectively. **c**. The photochemical rate corresponding to LEF and CEF can be estimated by measuring the initial slope of the ECS decay, as explained above (Bailleul et al, 2010; see Supplementary Information). Each point corresponds to 2-4 independent experiments (± S.D.). **d**. Light- dependencies of oxygen uptake (U_0, open circles) and gross photosynthesis (E_0, closed circles) in control conditions (dark) and in the presence of DCMU (red). Data are the average of two independent experiments (± S.D.).

Extended Data Fig. 3. ATP and photosynthesis under respiratory inhibition.

a. b. c. Dependency of the ETR_{PSII} (**a**), $\Delta\Psi_d$ (**b**) and dark respiration (**c**), expressed as a % of the untreated wt cells of *P. tricornutum*, following inhibition of the classical respiratory pathway with different concentrations of Antimycin A, in the presence of saturating SHAM (1000 µM). The experimental data were fitted by an exponential decay with the same decay constant in the three panels. **d. e. f.** Effect of AA, SHAM and AA+SHAM on dark respiration (**d**) $\Delta\Psi_d$ (**e**) and ETR_{PSII} (**f**), expressed as % of control, in wild-type cells of *P. tricornutum*. [SHAM]: 1mM. [AA]: 5µM. Data in all panels are the average of 2-4 independent experiments (± S.D.).

Extended Data Fig. 4. Dark respiration and ATP in AOX mutants in *P. tricornutum.*

a. Respiratory activity of wild type and AOX knockdown lines. Total respiration rate (red bars) and the contribution of the AOX capacity (white bars, see Supplementary Information) were normalized to wild-type values. Data are the average of at least 5 independent experiments (± S.D.). **b**. ECS-based measurements of $\Delta\Psi_{dark}$ in wild type and AOX knockdown lines, in control conditions (dark), in the presence of AA (grey), and in the presence of AA+SHAM (white). Data are the average of 2-3 independent experiments (± S.D.).

Extended Data Fig. 5. Subcellular localization of AOX in *P. tricornutum* and plastid-mitochondria interaction in *P tricornutum* wild-type cells.

a. Subcellular localization of AOX. Cells were treated with an anti-AOX antibody and then with a secondary Alexa Fluor 488 antibody (see Methods). Positions of plastid and nuclei are indicated by chlorophyll *a* autofluorescence (red) and DAPI staining (blue), respectively **b**. EM pictures of the plastid-mitochondria juxtaposition in *P. tricornutum*. Arrows indicate possible physical contacts between the plastid and mitochondrial membranes.

Extended Data Fig. 6. Growth and photoprotective responses in in Pt1 and AOX mutants.

a. Growth curves of wild type and AOX knockdown cell lines in the presence/absence of AA (2µM). AA was added every day and cells were grown in continuous light to prevent them from dying in the dark because of lack of respiration. Data are from 3 biological replicates (± S.D.). **b**. Light dependencies of NPQ in wild type and AOX knockdown mutants. Data are the average of 3 independent measurements (± S.D.).

Extended Data Fig. 7. Cytochrome *b_6f* turnover in Pt1 and AOX mutants.

a. Schematic representation of the electron flow reaction evaluated by the spectroscopic measurements. **b**. Slow phase of ECS_L indicating cytochrome *b_6* (blue) and time resolved redox changes of cytochrome *c/f* (red) in wild type Pt1 and AOX knockdown mutants**.** ***P. tricornutum*** cells were exposed to saturating single turnover laser flashes given 10 sec apart. Data were normalized to the amplitude of the fast phase of the ECS_{lin} signal. Cyt. *c* and ECS_{lin} were deconvoluted as explained in Methods. Traces represent 4 replicas from 2 biological samples (± S.D.). Cell concentration was 2* 10^{7} cells mL^{-1}. Note that both the slow phase of the ECS_{lin} and reduction of cytochrome c6/f were completely abolished by the plastoquinone competitive inhibitor DBMIB 10 µM (black arrow).

Extended Data Fig. 8. *In vivo* changes in the NADPH redox state and ATP in wild type and AOX knockdown mutants.

a. Changes in NADPH at different light intensities. Upward and downward arrows indicate when light was switched on and off, respectively. Light intensities were 50, 100, 200 and 400 µmol. photons m^{-2} s^{-1} (green, blue, red, and black traces, respectively). Chl concentration was ~5 µg mL-1. **b**. Representative spectra from cells of wild type (left panel) and AOX knockdown C5 (middle panel) and C9 (right panel) in the dark (red), light (green) and light + AA (blue) conditions are shown, with normalization to the internal standard (methylenediphosphonate; pH 8.9)). The positions of the α, β and γ phosphates of NTPs are shown. Inserts show the quantification of the NTP content in wild-type and AOX knockdown mutant cells, as reported in Fig. 3e (± S.D.).

Extended Data Fig. 9. **Cyclic electron flow in representative diatoms.**

a. Linear (closed circles) and cyclic (in the presence of DCMU) electron flows were measured at different light intensities, as in Extended Data Fig. 2, in *Thalassiosira weissflogii* (black), *Thalassiosira pseudonana* (blue) and *Fragilaria pinata* (red). **b**. CEF was plotted against LEF. The red line corresponds to CEF = 5% of the maximal LEF. Data are the average of 3-5 independent experiments (± S.D.).

Extended Data Fig. 10. ATP and photosynthesis under conditions of respiratory inhibition in representative diatoms.

Dark respiration (**a**, **b**, **c**, **d**), $\Delta\Psi_d$ (**e**, **f**, **g**, **h**) and ETR_{PSII} (**i**, **j**, **k**, **l**), in conditions of different levels of inhibition of the respiratory pathway with saturating Antimycin A, and/or saturating SHAM. Panels **a**, **e** and **i**: *T. weissflogii* (black). Panels **b**, **f** and **j**: *T. pseudonana* (blue). Panels **c**, **g** and **k**: *F. pinnata* (red). Panels **d**, **h** and **l**: *D. brightwelii* (green). Data in all panels are the average of 2-6 independent experiments (± S.D.).

Supplementary references

1- M, Vartanian, J, Desclés, M, Quinet, S, Douady, PJ, Lopez (2009) Plasticity and robustness of pattern formation in the model diatom *Phaeodactylum tricornutum*. New Phytol. **182**: 429–442.

2- RRL, Guillard (1975) Culture of phytoplankton for feeding marine invertebrates. pp 26-60. In Smith W.L. and Chanley M.H (Eds.) Culture of Marine Invertebrate Animals. Plenum Press, New York, USA.

3- B, Bailleul, P, Cardol, C, Breyton, G, Finazzi (2010) Electrochromism: a useful probe to study algal photosynthesis. Photosynth Res. **106**: 179-189.

4- S, Santabarbara, KE, Redding, F, Rappaport (2009) Temperature dependence of the reduction of p-700(+) by tightly bound plastocyanin *in vivo*. Biochemistry **48**: 10457–10466.

5- X, Johnson et al (2009) A new setup for *in vivo* fluorescence imaging of photosynthetic activity. J. Proteome Res. **10**: 5335-5338.

6- B, Genty, JM, Briantais, NR, Baker (1989) The relationship between the quantum yield of photosynthetic electron transport and quenching of chlorophyll fluorescence Biochim. Biophys. Acta **990**: 87-92.

7- C, Rivasseau et al (2009) Accumulation of 2-C-methyl-D-erythritol 2,4-cyclodiphosphate in illuminated plant leaves at supraoptimal temperatures reveals a bottleneck of the prokaryotic methylerythritol 4-phosphate pathway of isoprenoid biosynthesis. Plant Cell Environ. **32**: 82-92.

8- R, Bligny, R, Douce (2001) NMR and plant metabolism. Current Opinion Plant Biol. **4**: 191-196.

9- AML, Van de Meene, JD, Pickett-Heaps (2004) Valve morphogenesis in the centric diatom Rhizosolenia setigera (Bacillariophyceae, Centrales) and its taxonomic implications. European Journal of Phycology **39**: 93-104.

10- G, Peltier, P, Thibault (1985) O_2 uptake in the light in Chlamydomonas. Plant Physiol. **79**: 225–230.

11- TM, Kana et al (1994) Membrane inlet mass spectrometer for rapid and high-precision determination of N2,O2, and Ar in environmental water samples. Anal. Chem. **66**: 4166-4170.

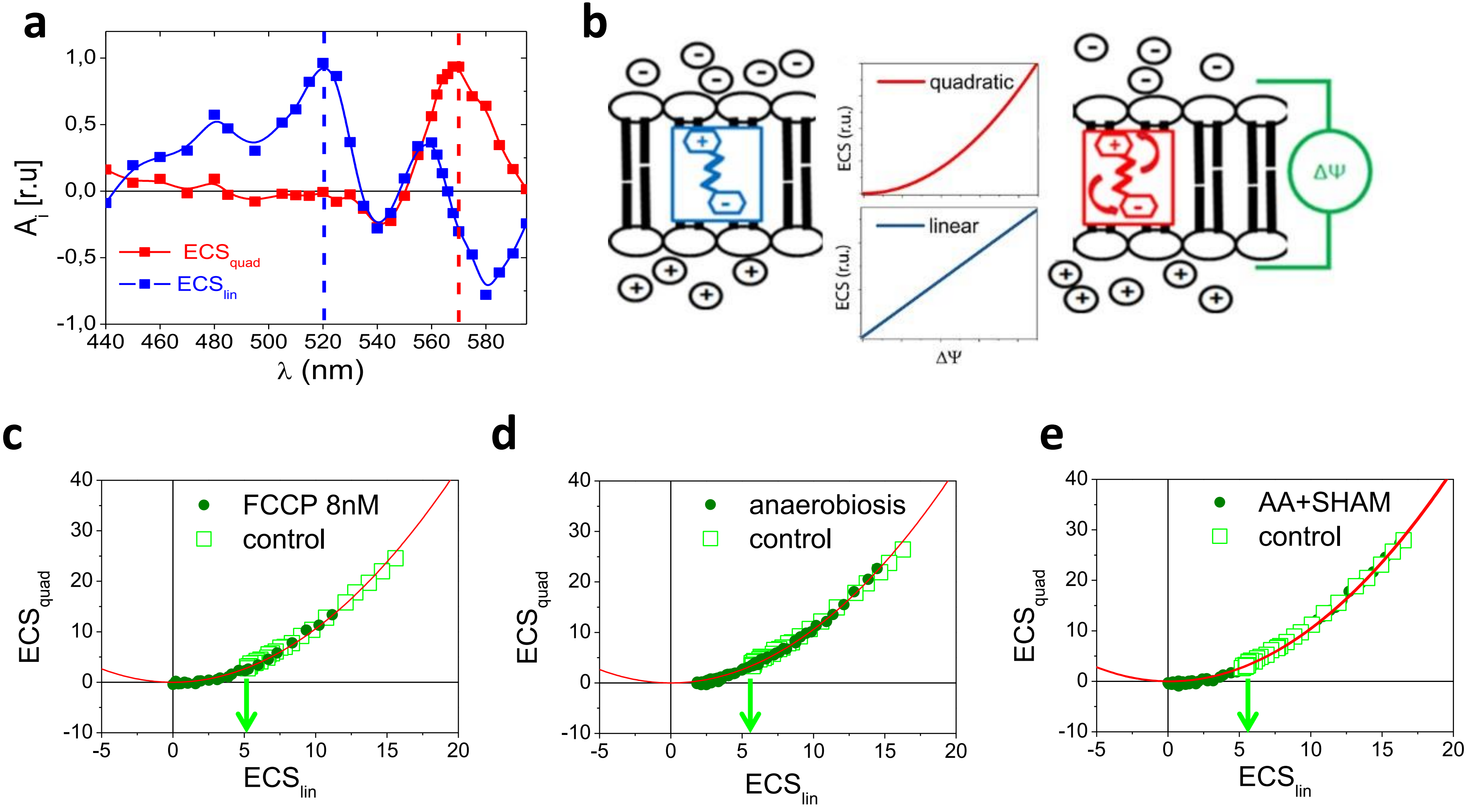

Figure 1. ECS provides an internal voltmeter in *P. tricornutum*

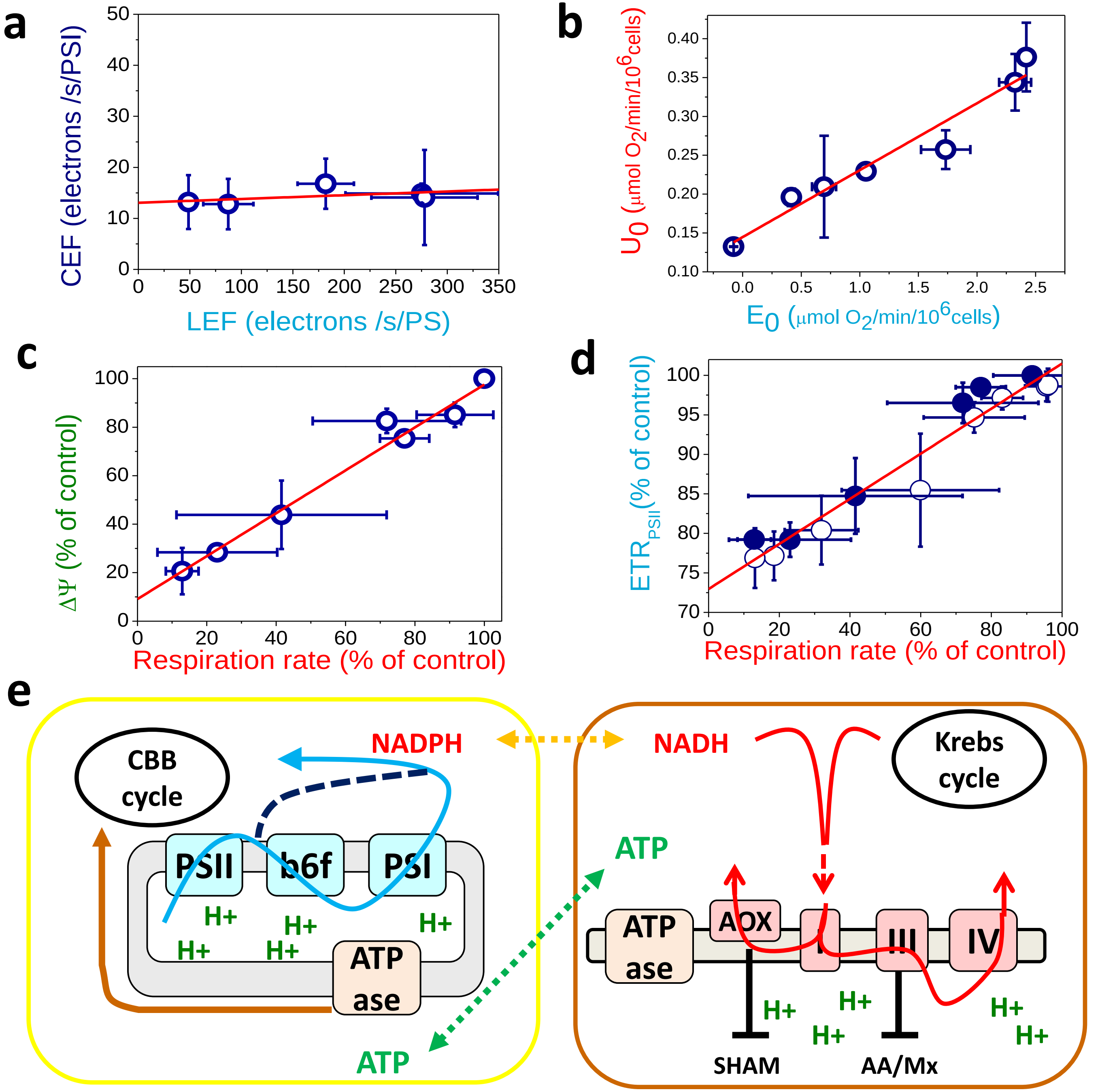

Figure 2. Mitochondria-plastid energetic interactions in *P. tricornutum*

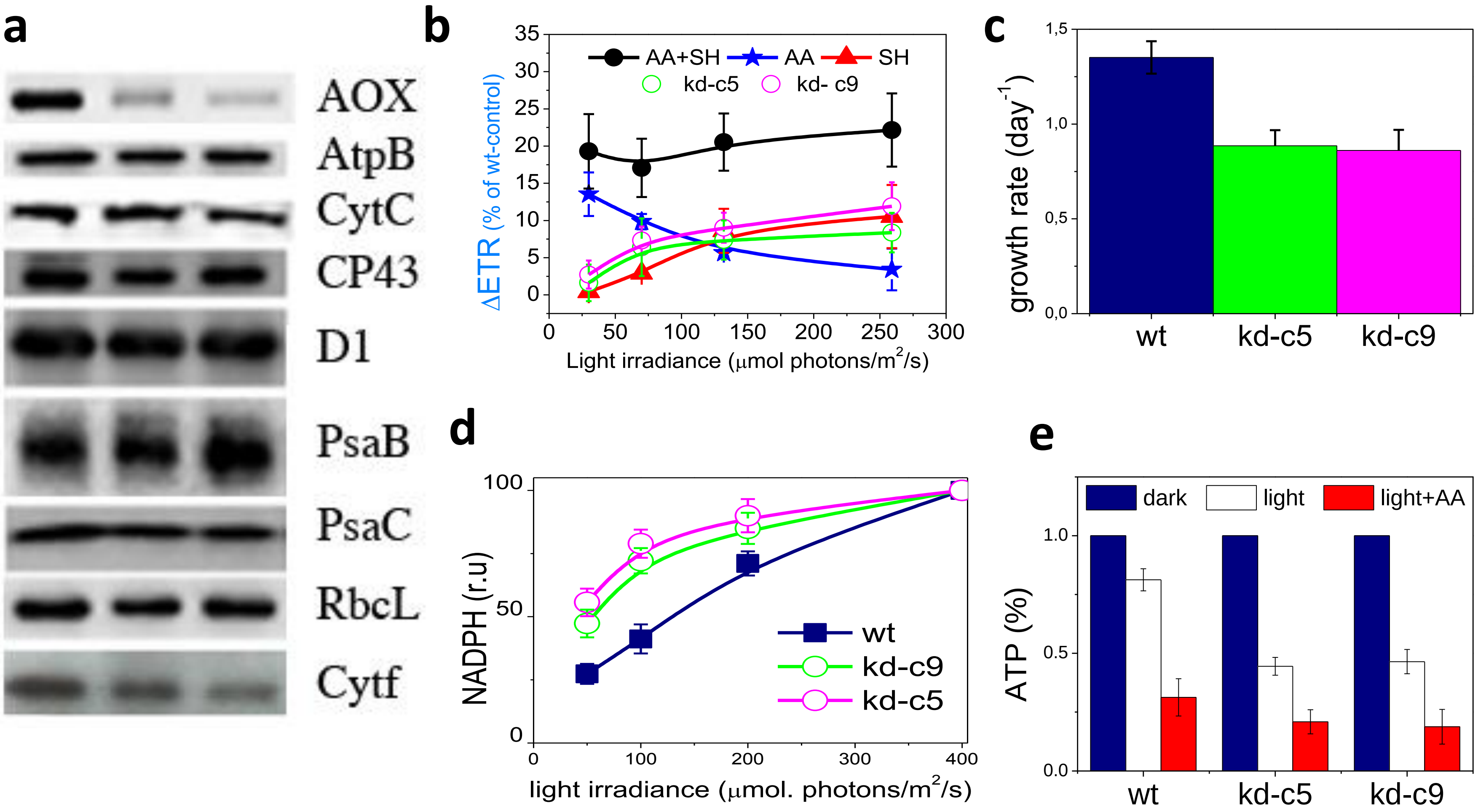

Figure 3. Phenotypic traits of AOX mutants in *P. tricornutum*

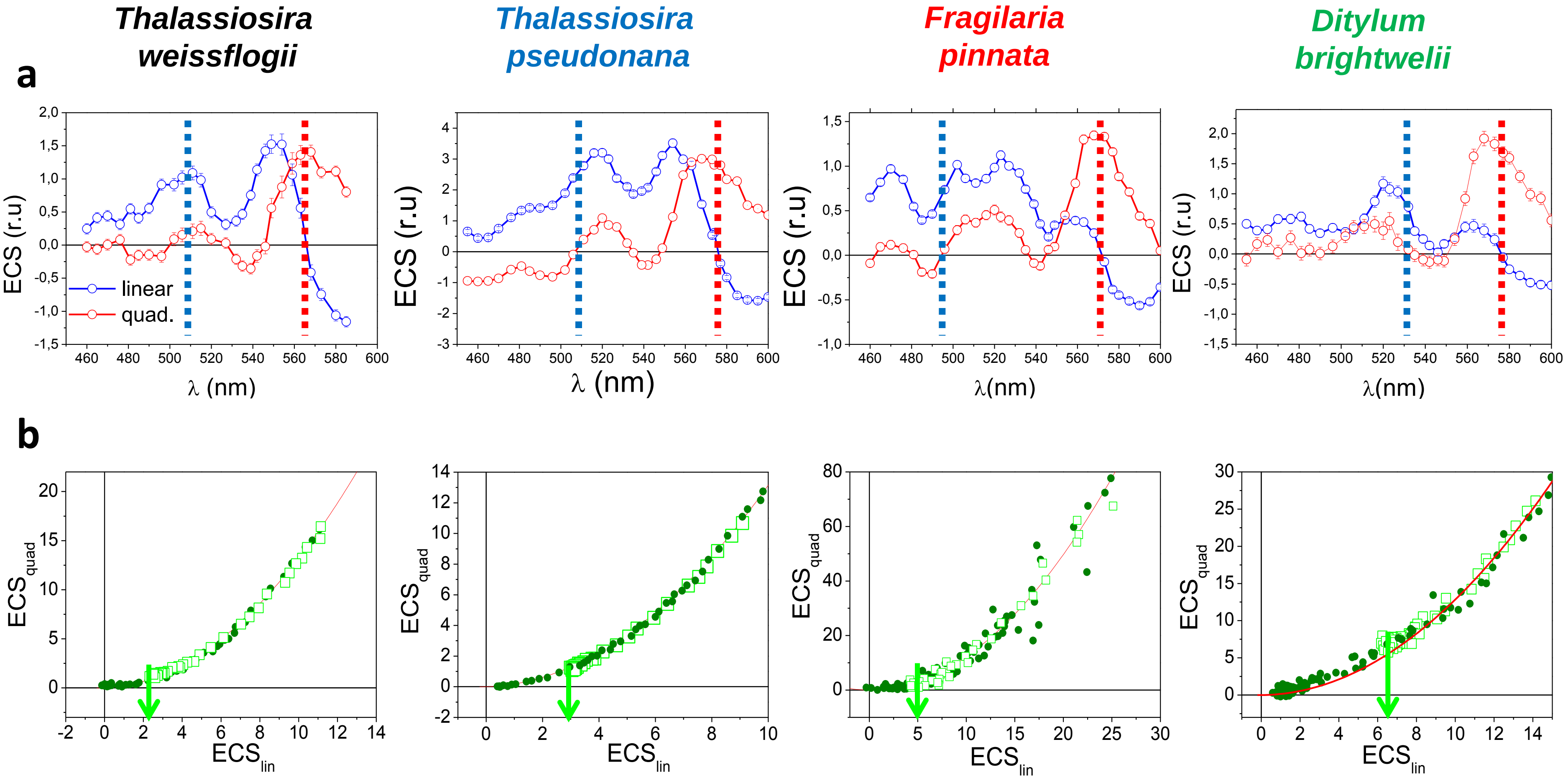

Figure 4: ATP transfer from mitochondria to plastid in representative diatoms

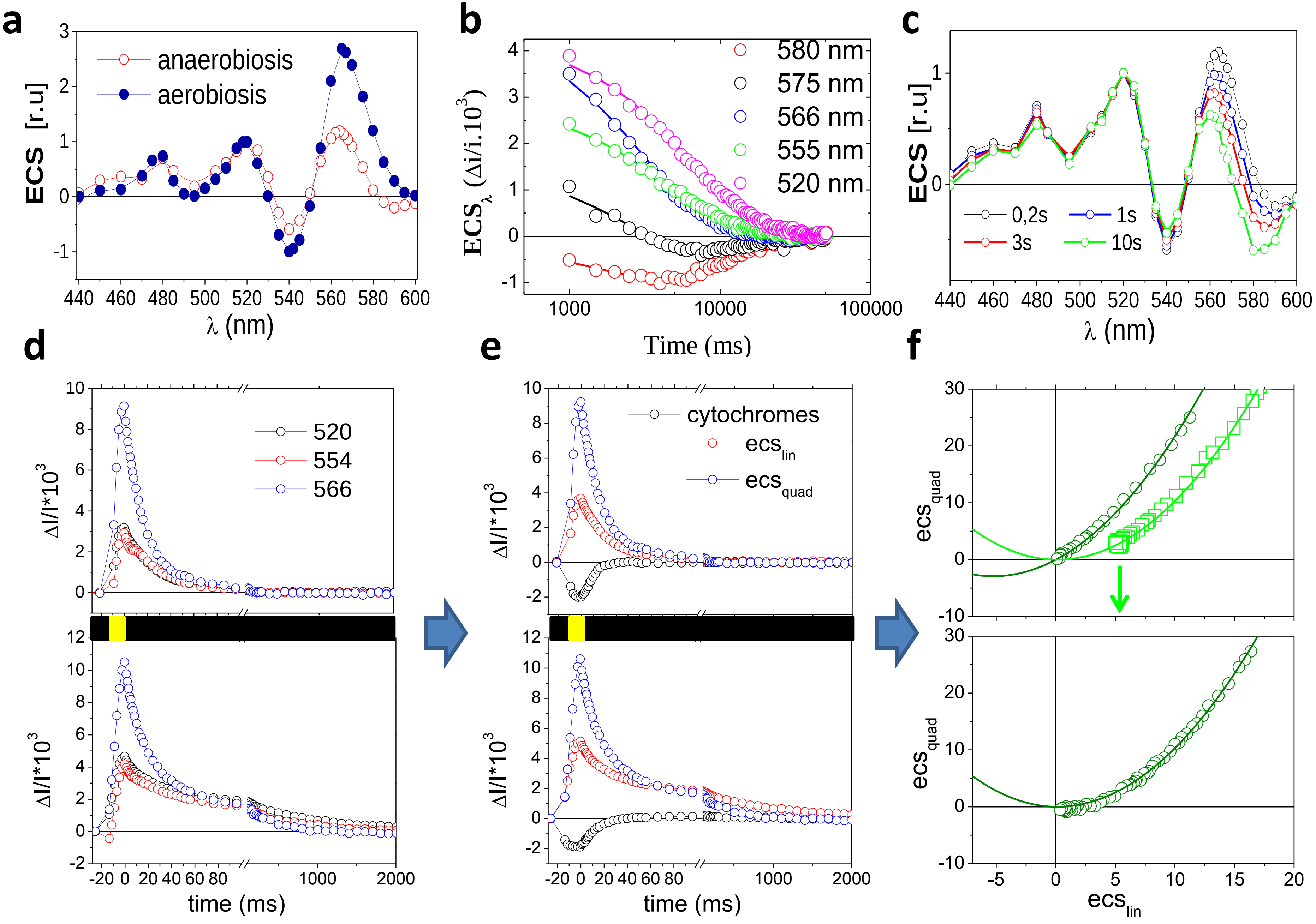

Extended data Figure 1. Characterization of the ECS-based internal voltmeter

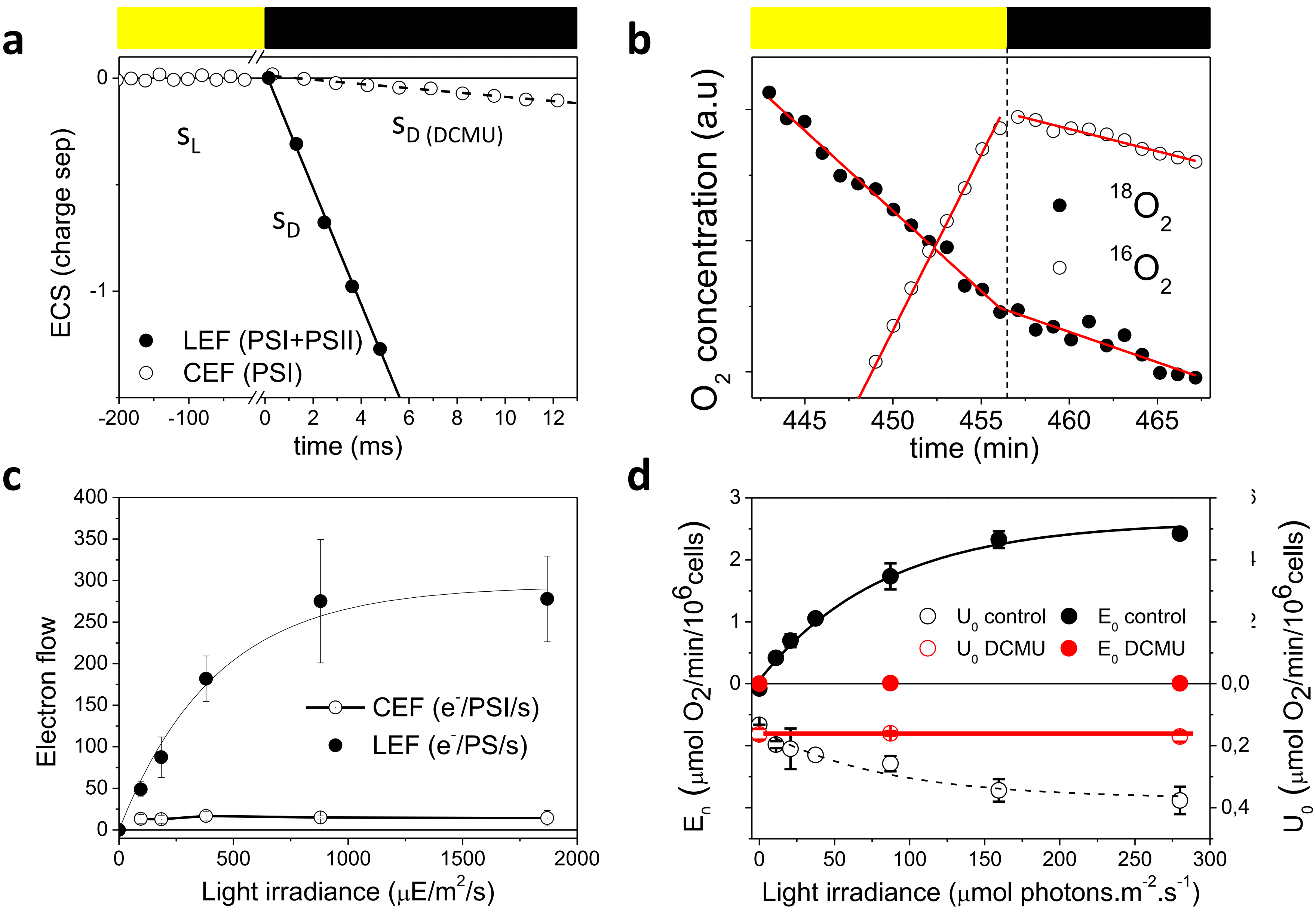

Extended Data Figure 2. Cyclic electron flow and water-to-water cycles in *P.tricornutum*

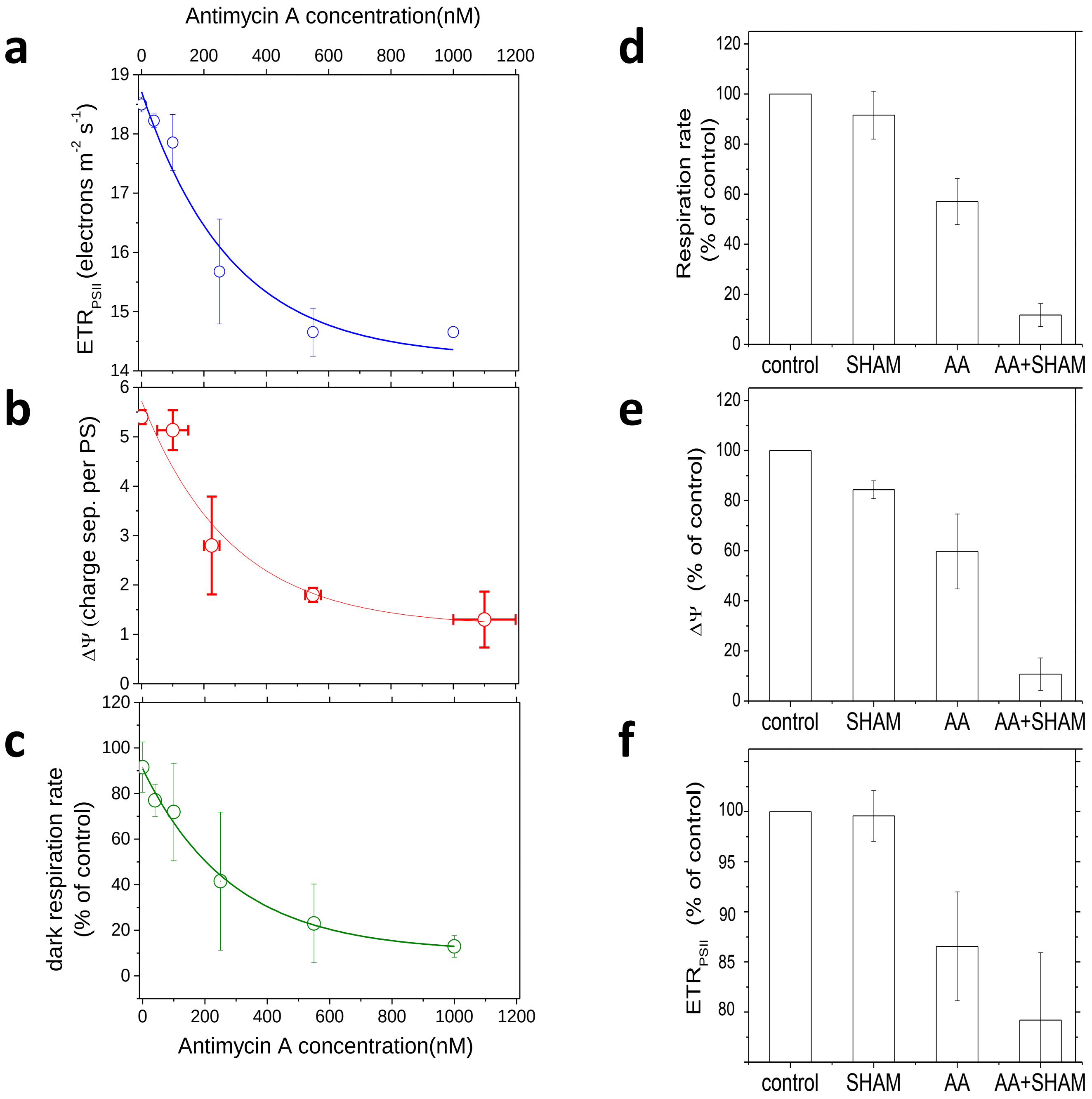

Extended Data Figure 3. ATP and photosynthesis under respiratory inhibition

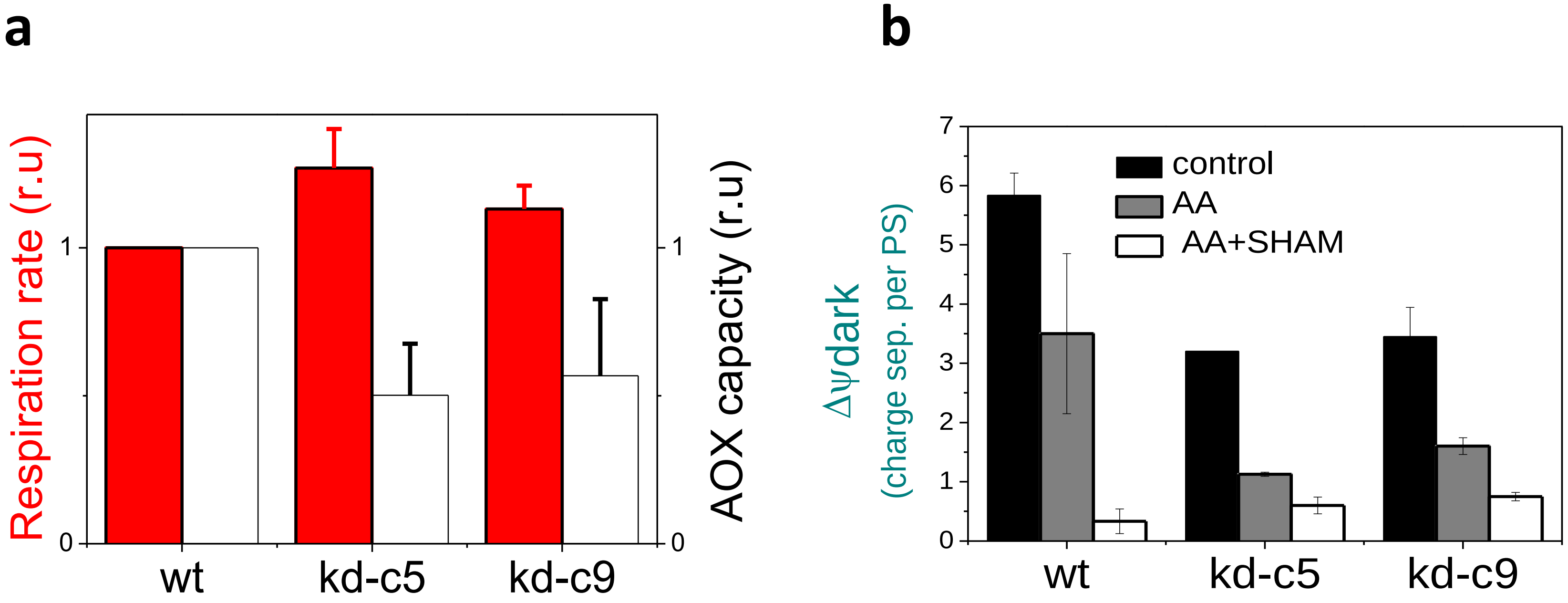

Extended Data Figure 4. Dark respiration and ATP in AOX mutants in *P. tricornutum*

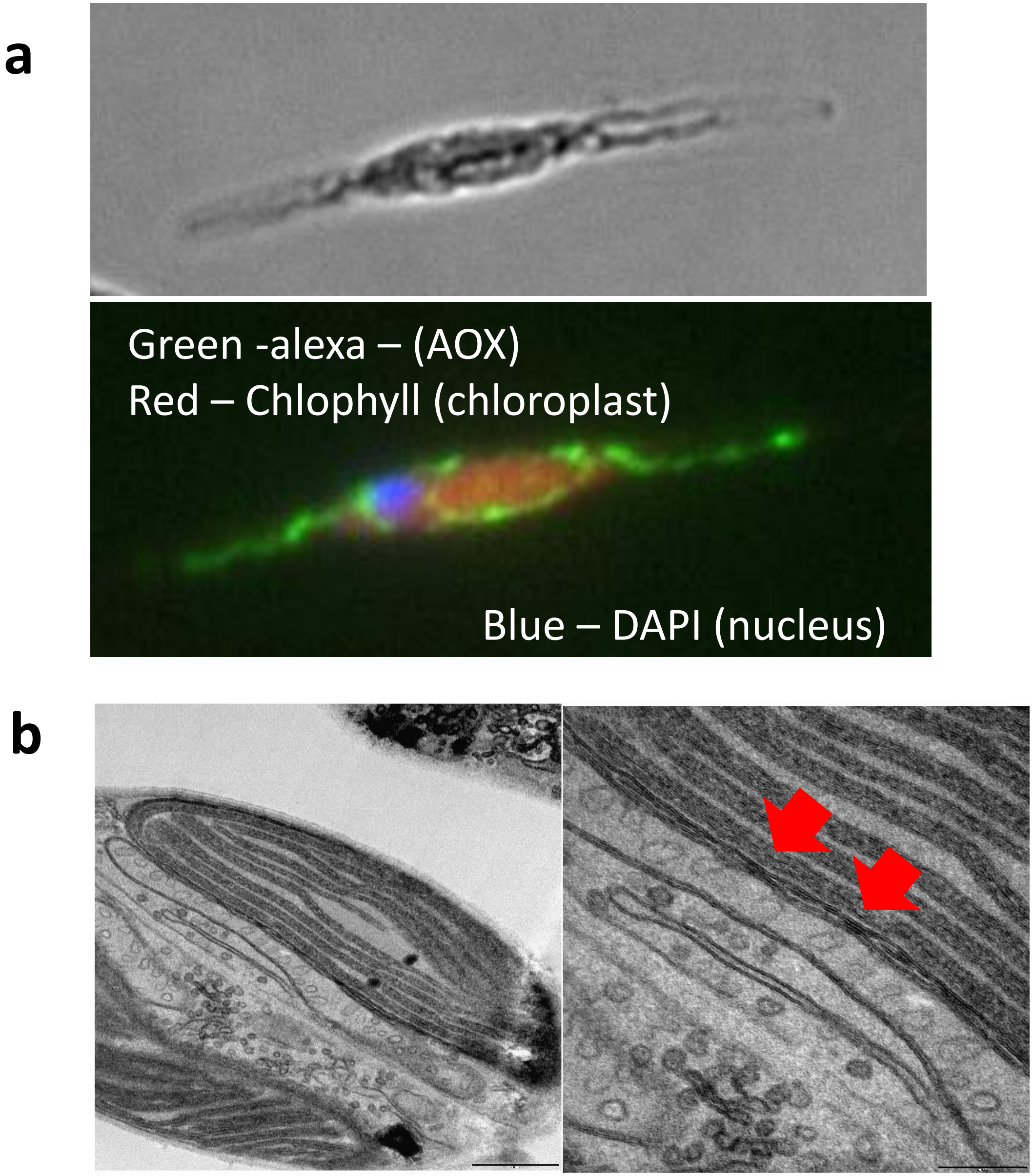

Extended Data Figure 5. Subcellular localization of AOX and plastid-mitochondria interaction in *P. tricornutum* wt cells.

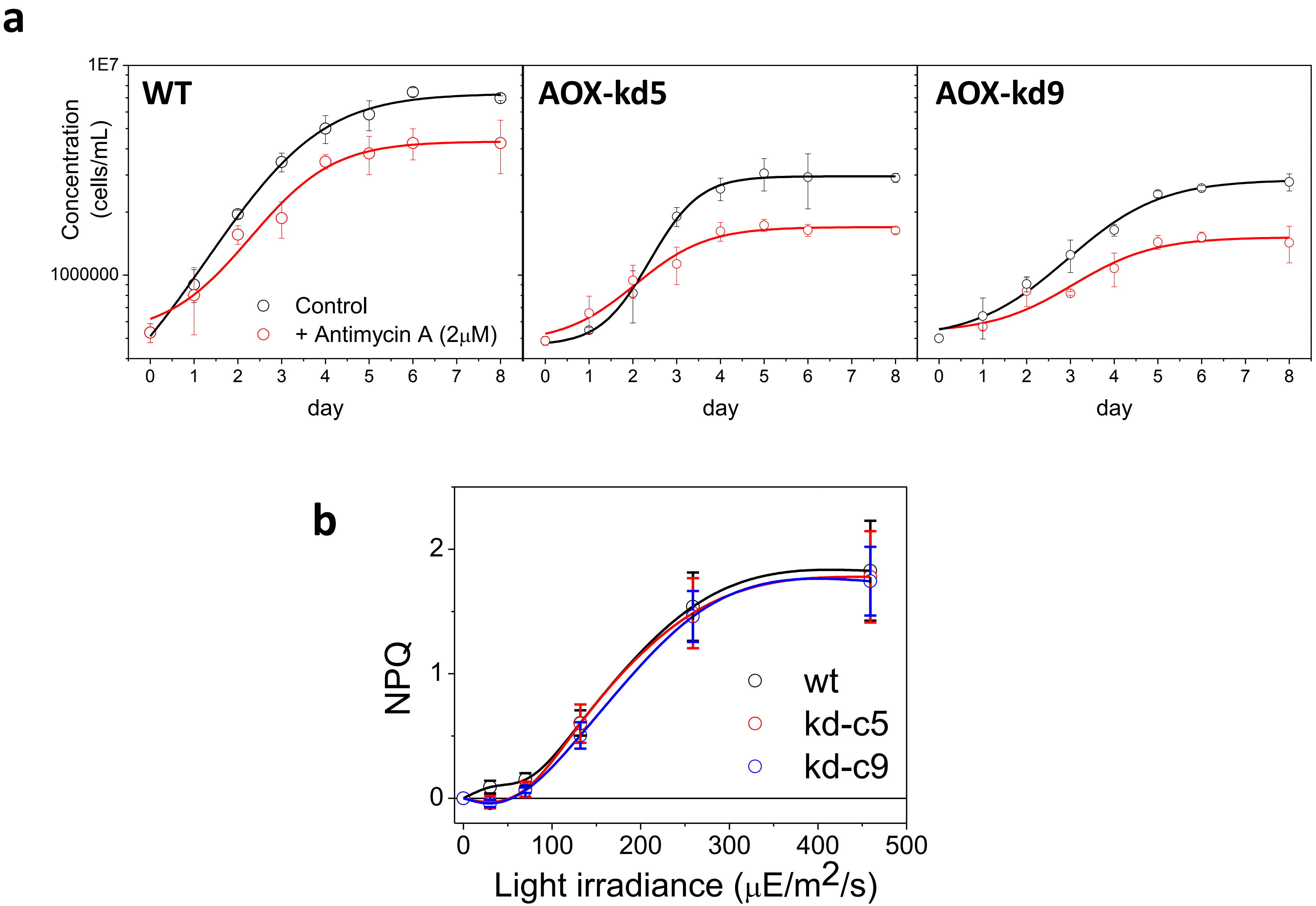

Extended Data Figure 6. Growth and photoprotective responses in *Pt1* and AOX mutants.

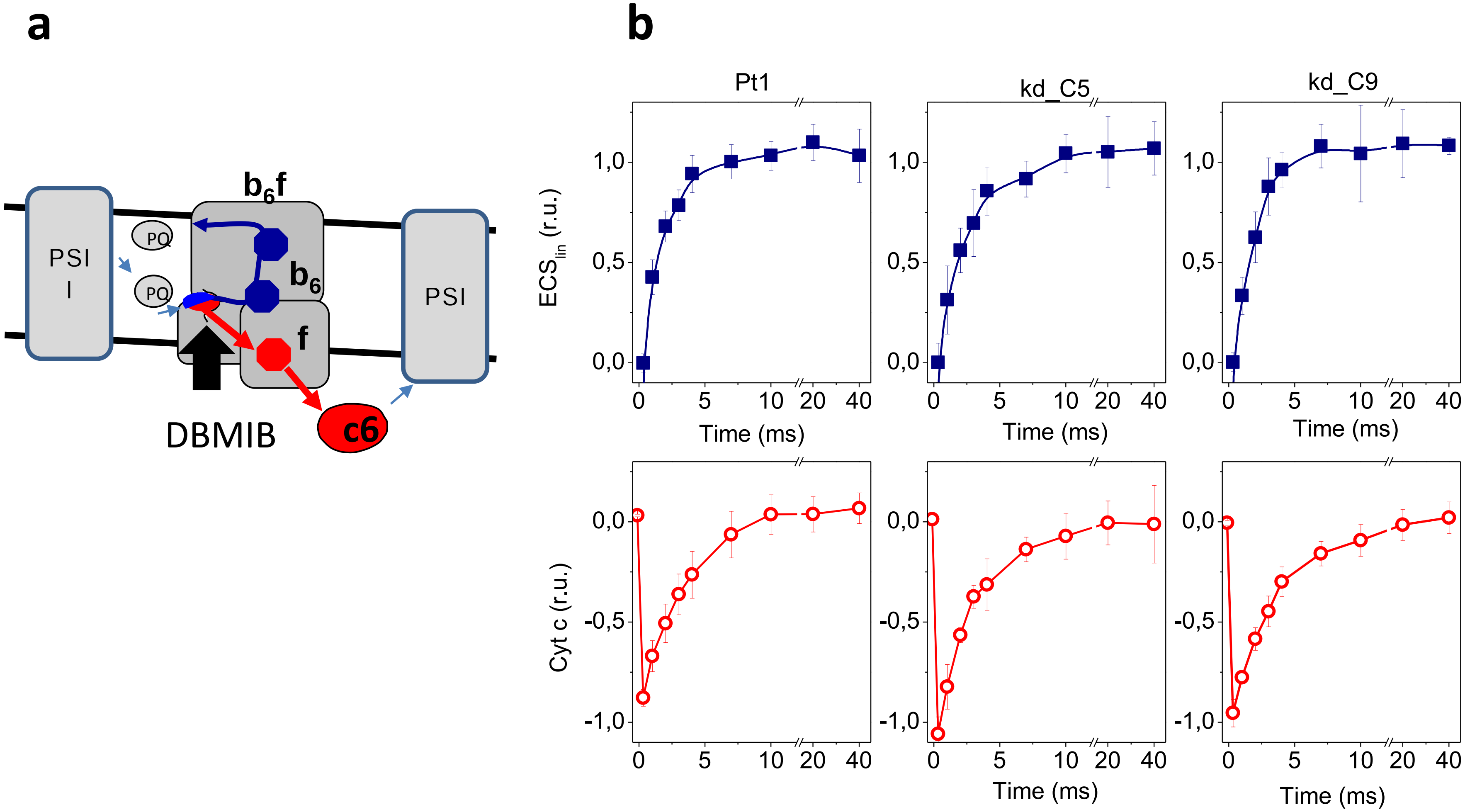

Extended Data Figure 7. cytochrome b6f turnover in Pt1 and AOX mutants.

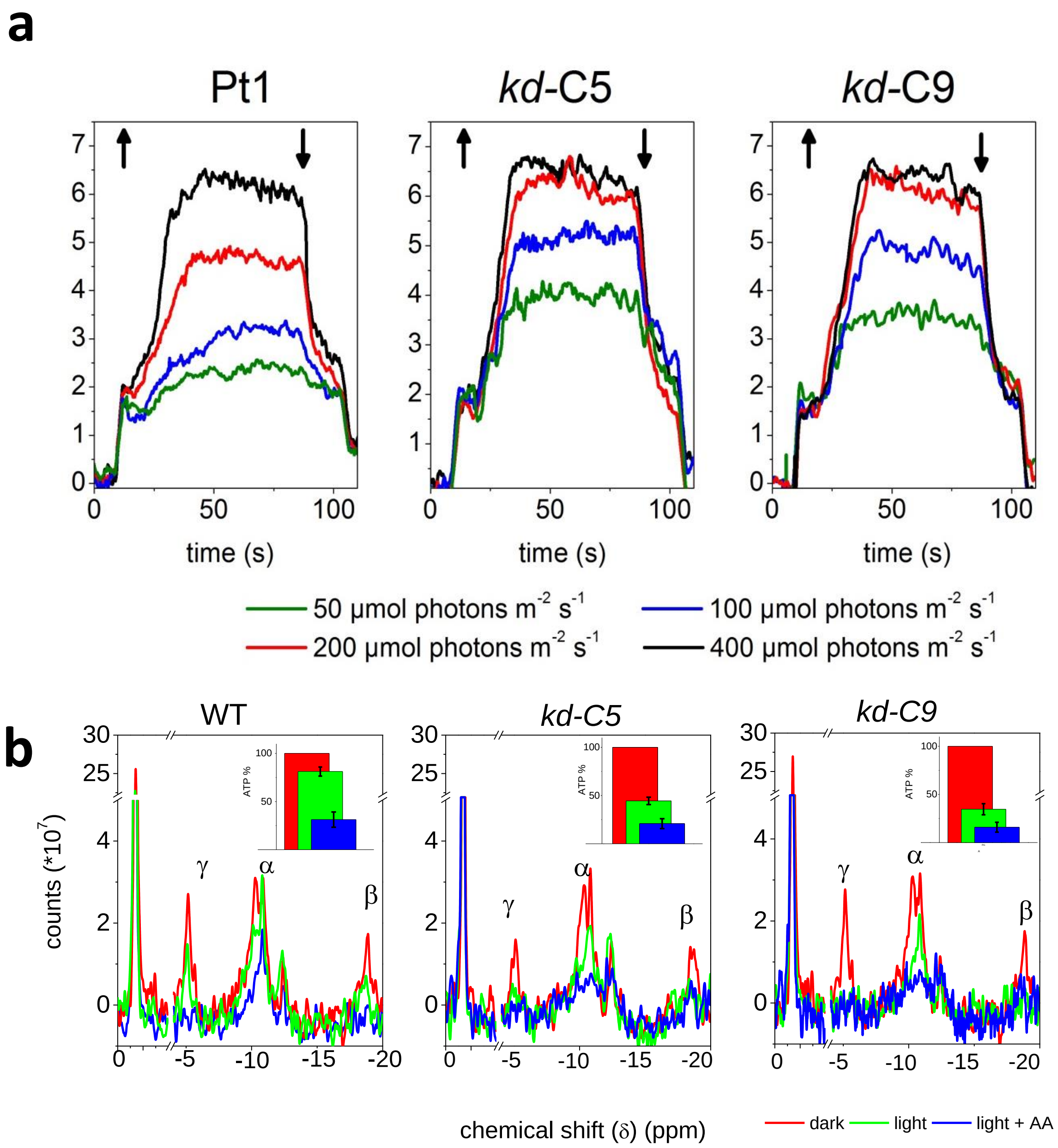

Extended Data Figure 8. *In vivo* changes in the NADPH redox state and ATP in wild type and AOX knockdown mutants.

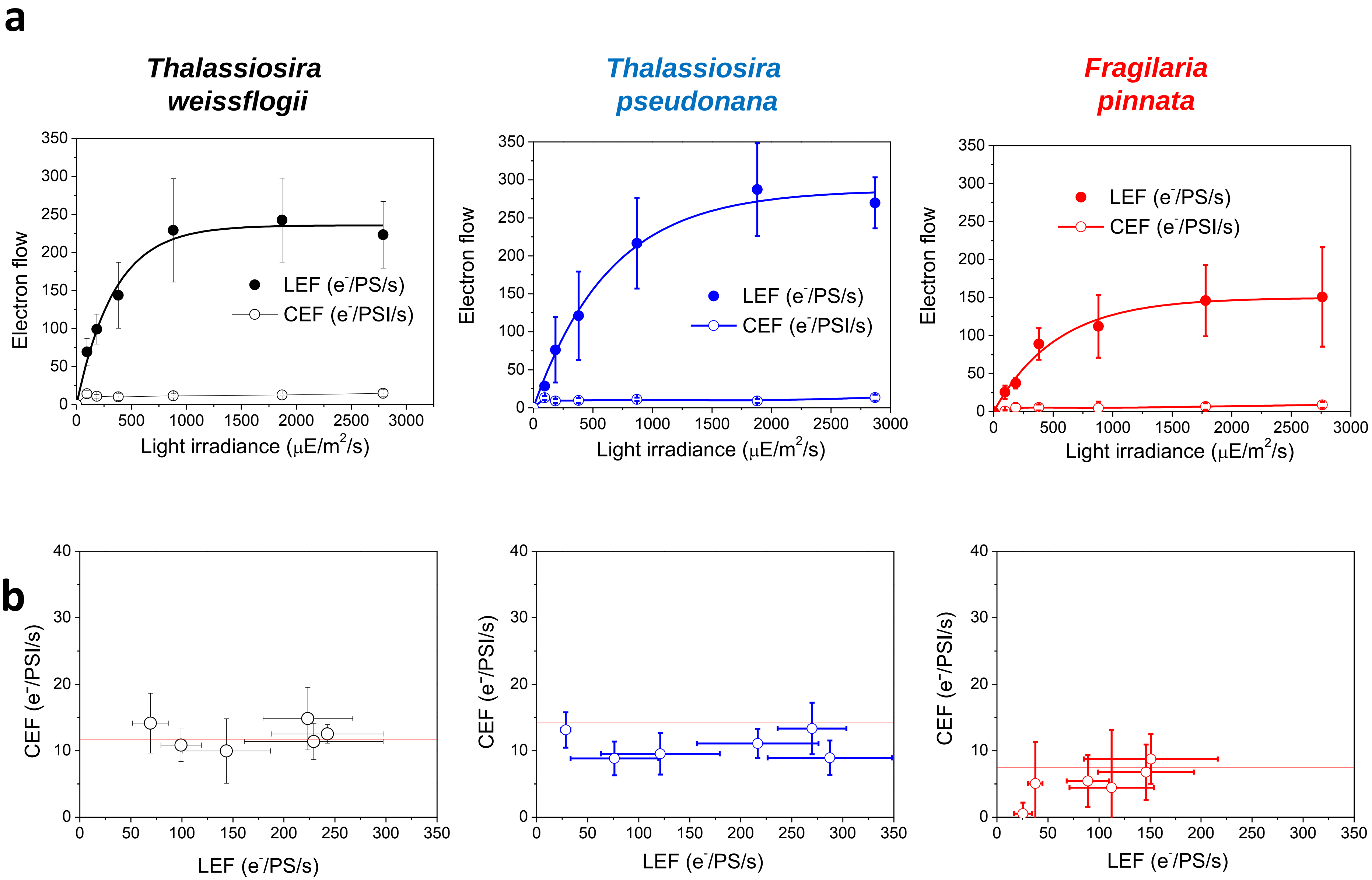

Extended Data Figure 9. Cyclic electron flow in representative diatoms

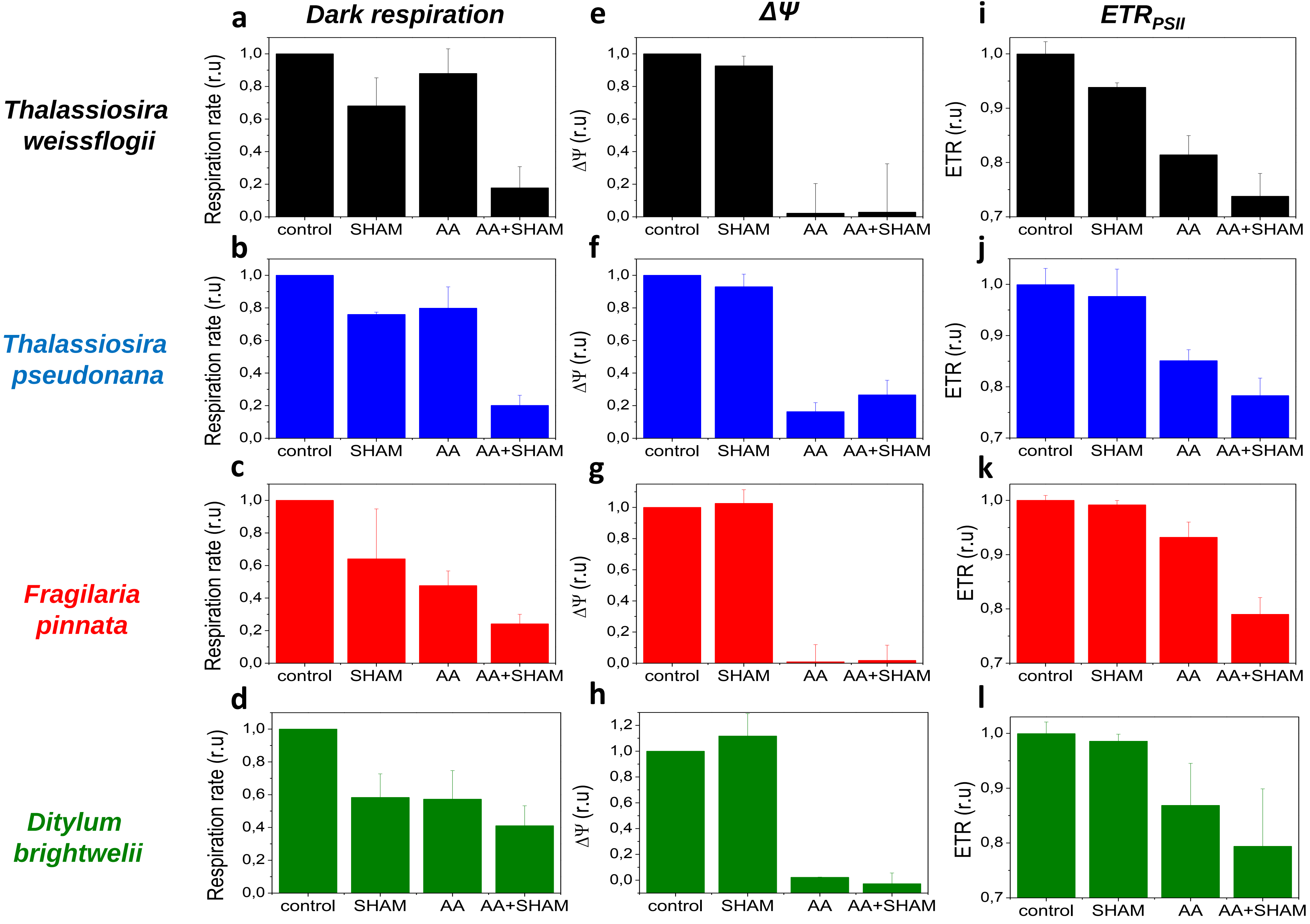

Extended Data Figure 10. ATP and photosynthesis under respiratory inhibition in representative diatoms